

## Ultrabroadband terahertz source and beamline based on coherent transition radiation

S. Casalbuoni,<sup>1</sup> B. Schmidt,<sup>2</sup> P. Schmüser,<sup>2,3</sup> V. Arsov,<sup>2</sup> and S. Wesch<sup>2</sup>

<sup>1</sup>*Institute for Synchrotron Radiation, Research Center Karlsruhe, P.O. Box 3640, D-76021 Karlsruhe, Germany*

<sup>2</sup>*Deutsches Elektronen-Synchrotron DESY, Notkestrasse 85, 22607 Hamburg, Germany*

<sup>3</sup>*Institut für Experimentalphysik, Universität Hamburg, Luruper Chaussee 149, 22607 Hamburg, Germany*

(Received 30 October 2008; published 25 March 2009)

Coherent transition radiation (CTR) in the THz regime is an important diagnostic tool for analyzing the temporal structure of the ultrashort electron bunches needed in ultraviolet and x-ray free-electron lasers. It is also a powerful source of such radiation, covering an exceptionally broad frequency range from about 200 GHz to 100 THz. At the soft x-ray free-electron laser FLASH we have installed a beam transport channel for transition radiation (TR) with the intention to guide a large fraction of the radiation to a laboratory outside the accelerator tunnel. The radiation is produced on a screen inside the ultrahigh vacuum beam pipe of the linac, coupled out through a diamond window and transported to the laboratory through an evacuated tube equipped with five focusing and four plane mirrors. The design of the beamline has been based on a thorough analysis of the generation of TR on metallic screens of limited size. The optical propagation of the radiation has been computed taking into account the effects of near-field (Fresnel) diffraction. The theoretical description of the TR source is presented in the first part of the paper, while the design principles and the technical layout of the beamline are described in the second part. First experimental results demonstrate that the CTR beamline covers the specified frequency range and preserves the narrow time structure of CTR pulses emitted by short electron bunches.

DOI: [10.1103/PhysRevSTAB.12.030705](https://doi.org/10.1103/PhysRevSTAB.12.030705)

PACS numbers: 41.60.Cr, 41.75.Ht, 41.85.Ew, 42.81.Gs

### I. INTRODUCTION

In this paper, we describe a coherent transition radiation beamline that has been installed in the straight section between the superconducting linac and the undulator magnet system of the free-electron laser (FEL) facility FLASH. In the following we call it the coherent transition radiation (CTR) beamline. It has been specifically designed to accept a very large bandwidth ranging from about 200 GHz up to optical frequencies. While the main task of the CTR beamline is high-resolution longitudinal electron bunch diagnostics, it may equally well serve as a powerful and broadband source of THz radiation for experiments that can be performed in a laboratory outside the accelerator tunnel, providing pulse energies of more than 10  $\mu\text{J}$  in a frequency band from 200 GHz to about 100 THz.

For almost two decades, coherent transition radiation in the far-infrared regime has been established as a tool for longitudinal electron beam diagnostics. The first observation of CTR was reported in the early 1990s [1,2]. A particularly interesting application was the reconstruction of a longitudinally asymmetric electron bunch shape by measuring the far-infrared CTR spectrum with a polarizing Michelson spectrometer and determining the phase of the bunch form factor with the help of the Kramers-Kronig dispersion relation [3]. The use of far-infrared CTR for longitudinal bunch shape analysis was investigated in [4,5].

In case of forward transition radiation (TR) the so-called *formation length*  $L_f$ , i.e., the length needed to separate the self-field of the electron from the emitted electromagnetic

wave, plays an important role. It can be defined as the length in which the radiated wave advances by one wavelength  $\lambda$  with respect to the electron [6]. For radiation observed at an angle  $\theta$  with respect to the electron direction, one gets

$$L_f = \frac{\lambda}{1 - \beta \cos\theta} \approx \frac{2\gamma^2 \lambda}{1 + \gamma^2 \theta^2}, \quad (1)$$

where  $\beta = v/c$  is the scaled particle velocity and  $\gamma = 1/\sqrt{1 - \beta^2}$  the Lorentz factor. For typical emission angles  $\theta \leq 1/\gamma$  the formation length is  $L_f \approx \gamma^2 \lambda$  and thus many orders of magnitude larger than the wavelength. Within the formation length, forward TR is partially suppressed [4].

The situation is quite different for TR in the backward hemisphere. Here the formation length is  $L_f \approx \lambda/2$  and thus very short because electron and radiation move in opposite directions. Our CTR beamline utilizes radiation in the backward hemisphere; therefore the formation length is of no importance. The same applies to the majority of CTR-based longitudinal beam diagnostics experiments, see e.g. [3,7–13].

The main goal in designing and constructing a CTR beamline was to facilitate longitudinal bunch diagnostics using detectors outside the accelerator tunnel of FLASH since the access to the linear accelerator is extremely limited during the extended periods of FEL user operation. A second goal was to provide a broadband source of intense THz radiation for the development of new detec-

tion schemes and spectroscopic methods as well as for dedicated THz experiments.

More than 20 beamlines have been built in accelerators worldwide to extract infrared (IR), respectively terahertz radiation, for user operation [14]. The traditional source of the IR beamlines is synchrotron radiation from a bending magnet [15–17]. Interest in increasing infrared output has led to the use of edge radiation [18–23] and undulator radiation [24,25].

Narrowband THz sources can be realized using FEL technology. At the infrared FEL FELIX [26], the frequency can be varied between 1.2 and 100 THz and the pulse energy is in the range 1–50  $\mu\text{J}$ . A recent narrowband source is the infrared undulator beamline at FLASH [25] which can be tuned from 1.5 to 300 THz with pulse energies between 7 and 20  $\mu\text{J}$ .

Broadband THz sources are often based on coherent synchrotron radiation (CSR) by short electron bunches passing a bending magnet. The frequency range covered by CSR in storage rings (BESSY, ALS, NSLS, ANKA, CLS, MAX-I, ELETTRA, New SUBARU) goes up to 1–2 THz. Steady-state CSR has been achieved at BESSY [27] and ANKA [28]. The most powerful broadband THz source is the energy recovery linac at Jefferson Laboratory with pulse energies up to 300  $\mu\text{J}$  and frequencies up to 2 THz [29]. We will demonstrate that the CTR beamline at FLASH has the unique feature of extending the range to far higher frequencies, owing to the extreme shortness and substructure of the compressed electron bunches and the broadband transmission characteristics of the beam transport system.

Transition radiation (TR) is emitted when a relativistic charged particle crosses the boundary between two media of different dielectric properties. For a planar boundary of infinite extent, the well-known Ginzburg-Frank (GF) formula holds which, however, is not applicable in many practical cases because two basic conditions of the analytic derivation are often not fulfilled: the radiation screens used in an accelerator are of limited size, and the radiation is usually observed in the near-field and not in the far-field diffraction regime. Following [30,31], we apply the Weizsäcker-Williams method of virtual quanta for computing backward TR from a finite metallic screen. We will prove that perfect agreement with the GF equation is obtained if the screen size tends to infinity. Moreover, we will show how the virtual-quanta method can be used to compute TR emitted from a screen of arbitrary size and shape and observed at any distance from the source. Hence, the method is well suited for realistic experimental setups.

The paper is organized as follows. In Sec. II we present the theoretical description of the transition radiation source. The Ginzburg-Frank formula is generalized to the case of a radiation screen of finite size. The corrections due to near-field diffraction effects are studied. The results obtained in Sec. II are the basis for the design and practical

realization of the CTR beamline at FLASH which is described in Sec. III. First measurements with the CTR beamline are reported in Sec. IV.

## II. THEORETICAL DESCRIPTION OF THE TRANSITION RADIATION SOURCE

### A. Ginzburg-Frank formula

The standard theory of transition radiation can be found in [32]. The Maxwell equations are solved for a relativistic electron approaching a planar boundary between two media of different dielectric constants. The electromagnetic field carried by the particle changes when going from one medium to the other. To satisfy the boundary conditions for the electric and magnetic field vectors one has to add two radiation fields, propagating in the forward, respectively the backward, direction. The spectral and spatial radiation energy of backward TR, emitted by an electron hitting an infinite metallic screen of perfect reflectivity, is given by the Ginzburg-Frank (GF) formula which reads in SI units

$$\frac{d^2 U_{\text{GF}}}{d\omega d\Omega} = \frac{e^2}{4\pi^3 \epsilon_0 c} \frac{\beta^2 \sin^2 \theta}{(1 - \beta^2 \cos^2 \theta)^2}, \quad (2)$$

where  $\theta$  is the angle measured against the backward direction. This formula holds for normal incidence and is valid in the far field only. A characteristic feature is the vanishing intensity in the exact backward direction at  $\theta = 0$  which is caused by destructive interference due to the radial polarization of the radiation. The angular distribution has its maximum at the angle  $\theta_{\text{max}} \simeq 1/\gamma$ .

For an infinite screen, the spectral TR energy (2) does not depend on the angular frequency  $\omega$ , provided one stays well below the plasma frequency of the metal. In Sec. II C we will show that for a finite TR screen the radiation energy acquires an  $\omega$  dependence.

### B. Weizsäcker-Williams method of virtual quanta

The boundary-condition method can be generalized to describe the radiation from screens of other shapes, e.g., a circular disk, a circular hole in an infinite plane, or a semi-infinite half plane [33,34]. This will not be discussed here because the mathematical effort is considerable and the results apply only for far-field diffraction. Radiation from a screen of arbitrary shape cannot be calculated analytically. An alternative approach to compute the radiation by a relativistic charged particle at the transition from vacuum to a metal is based on the Weizsäcker-Williams method of virtual quanta, see e.g. [6,35]. The assumption is made that the *virtual photons*, constituting the self-field of the particle, are converted into *real photons* by reflection at the metallic interface. Effectively this means that the Fourier components of the transverse electric field of the electron are reflected at the metal surface. Then the Huygens-Fresnel principle is applied to compute the outgoing electromagnetic wave. An important prerequisite is the fact

that the electromagnetic field of a highly relativistic electron is concentrated in a flat disk perpendicular to the direction of motion and is thus essentially transverse. An equivalent approach to compute TR [36] is based on the observation that the transient azimuthal magnetic field of the relativistic electron induces time-dependent radial currents in the metallic screen which are then the source of the emitted radiation field.

### C. Generalization of the Ginzburg-Frank formula

In this section we apply the virtual-quanta method to compute backward TR from a finite screen. For the special case of a circular disk hit by a particle in its center at normal incidence the computation can be done analytically. We will follow the treatment of Ref. [31], and demonstrate that the GF formula results if the disk radius tends to infinity and the radiation is observed at a large distance from the source. For screens of other shapes, the Fourier transform method outlined in Ref. [37] is adequate.

#### 1. Computation of field on observation screen

We take a metallic disk of radius  $a$  as our TR source and use cylindrical coordinates  $(\rho, \phi, z)$ . The longitudinal position of the disk is  $z = 0$ . The observation screen is placed at a distance  $D \gg a$  from the TR source. The Fourier component  $\tilde{E}_r$  of the radial electric field of the incident electron is given by

$$\tilde{E}_r(\rho, \omega) = \frac{-e\omega}{(2\pi)^{3/2}\epsilon_0\beta^2\gamma c^2} K_1\left(\frac{\omega\rho}{\beta\gamma c}\right), \quad (3)$$

where  $K_1$  is the modified Bessel function [compare Eq. (13.80) in Jackson [35]]. Because of the cylindrical symmetry, the field on the observation screen will be radial as well. Without loss of generality we can therefore choose our target point to be located on the  $x$  axis of the observation screen:  $P = (x, y = 0, z = D)$ . The geometry is sketched in Fig. 1. The electric field at  $P$  will then have an  $x$  component only. A small area element at an arbitrary

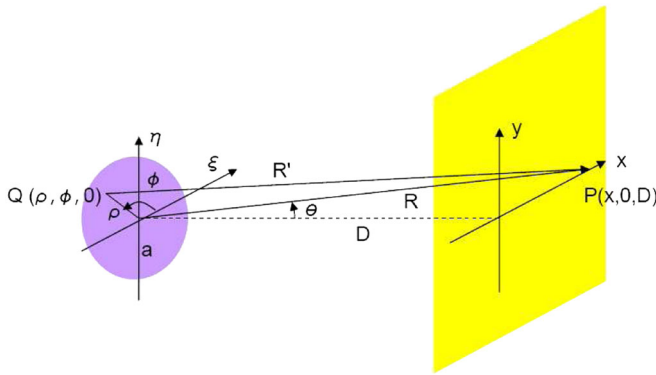


FIG. 1. (Color) Diffraction geometry for a finite TR source (metallic screen with radius  $a$ ) and an observation screen placed at a distance  $D \gg a$ .

point  $Q = (\rho, \phi, 0)$  of the TR source screen at  $z = 0$  yields the following contribution to the horizontal field component at  $P$ :

$$d\tilde{E}_x(P, \omega) = -\frac{ik}{2\pi} \tilde{E}_r(\rho, \omega) \cos\phi \frac{\exp(ikR')}{R'} \rho d\rho d\phi,$$

where  $R' = \sqrt{D^2 + (x - \rho \cos\phi)^2 + (\rho \sin\phi)^2}$  is the distance between  $Q$  and  $P$  and  $k = \omega/c$ . The electric field at  $P$  is given by integration over the TR source

$$\tilde{E}_x(P, \omega) = -\frac{ik}{2\pi} \int_0^a \int_0^{2\pi} \tilde{E}_r(\rho, \omega) \times \cos\phi \frac{\exp(ikR')}{R'} d\phi \rho d\rho. \quad (4)$$

The square root is expanded up to second order in  $\rho$ :

$$R' = \sqrt{D^2 + (x - \rho \cos\phi)^2 + (\rho \sin\phi)^2} \approx R - \frac{x\rho \cos\phi}{R} + \frac{\rho^2}{2R} \quad (5)$$

with  $R = \sqrt{D^2 + x^2}$ . The second term in (5) is responsible for far-field (Fraunhofer) diffraction while the third term accounts for the near-field effects (Fresnel diffraction).

We consider first the far-field case and neglect the term  $\rho^2/(2R)$ . The distance  $R' = \overline{QP}$  in the denominator of the integrand of Eq. (4) can be replaced by the distance  $R$  between the center of the TR screen and the observation point  $P$ ; hence,

$$\frac{\exp(ikR')}{R'} \approx \frac{\exp(ikR)}{R} \exp(-ik\rho \sin\theta \cos\phi), \quad (6)$$

where the angle  $\theta$  is defined by  $\sin\theta = x/R$ .

Using Eqs. (3) and (4), the field at the observation point  $P = (x, 0, D)$  is written as

$$\tilde{E}_x(P, \omega) = \frac{iek^2}{(2\pi)^{5/2}\epsilon_0\beta^2\gamma c} \frac{\exp(ikR)}{R} \times \int_0^a \left[ \int_0^{2\pi} K_1\left(\frac{k\rho}{\beta\gamma}\right) \cos\phi e^{-ik\rho \sin\theta \cos\phi} d\phi \right] \rho d\rho.$$

The integration over the azimuthal angle yields the Bessel function  $J_1$

$$\int_0^{2\pi} e^{-ik\rho \sin\theta \cos\phi} \cos\phi d\phi = -2\pi i J_1(k\rho \sin\theta).$$

The remaining integration over the radius  $\rho$  can be carried out analytically. Making the replacement  $k = \omega/c$ , one gets

$$\int_0^a J_1\left(\frac{\omega\rho \sin\theta}{c}\right) K_1\left(\frac{\omega\rho}{c\beta\gamma}\right) \rho d\rho = \frac{\beta^3 c^2 \gamma \sin\theta}{\omega^2 (1 - \beta^2 \cos^2\theta)} [1 - T(\gamma, \omega a, \theta)] \quad (7)$$

with the correction term

$$T(\gamma, \omega a, \theta) = \frac{\omega a}{c\beta\gamma} J_0\left(\frac{\omega a \sin\theta}{c}\right) K_1\left(\frac{\omega a}{c\beta\gamma}\right) + \frac{\omega a}{c\beta^2\gamma^2 \sin\theta} J_1\left(\frac{\omega a \sin\theta}{c}\right) K_0\left(\frac{\omega a}{c\beta\gamma}\right). \quad (8)$$

The correction term depends on the Lorentz factor  $\gamma$ , the product of angular frequency and screen radius  $\omega a$ , and the observation angle  $\theta$ . The Fourier-transformed electric field on the observation screen becomes

$$\tilde{E}_x(\theta, \omega) = \frac{e}{(2\pi)^{3/2} \epsilon_0 c} \frac{e^{ikR}}{R} \frac{\beta \sin\theta}{1 - \beta^2 \cos^2\theta} [1 - T(\gamma, \omega a, \theta)]. \quad (9)$$

## 2. Generalized Ginzburg-Frank formula

For a conventional plane electromagnetic wave, the radiated spectral energy density is calculated from the Fourier components of the field in the following way:

$$\frac{dU}{d\omega} = \frac{2}{\mu_0 c} |\tilde{E}(\omega)|^2 = 2\epsilon_0 c |\tilde{E}(\omega)|^2. \quad (10)$$

In transition radiation, the field depends not only on frequency but also on the observation angle  $\theta$ . Putting (9) into Eq. (10) and keeping in mind that the area element  $dS$  at the observation point  $P$  is  $dS = R^2 d\Omega$ , we obtain for the spectral energy as a function of the angle  $\theta$

$$\frac{d^2 U_{\text{disk}}}{d\omega d\Omega} = \frac{d^2 U_{\text{GF}}}{d\omega d\Omega} [1 - T(\gamma, \omega a, \theta)]^2. \quad (11)$$

Equation (11) is the generalization of the GF formula for a TR source having the shape of a disk of radius  $a$ . A similar expression has been reported in Ref. [31]. Note that the generalized GF formula is only valid in the far-field regime because in the derivation we have used first-order Taylor expansion of the distance  $R'$ . Furthermore the metallic screen must have perfect reflectivity at the frequencies under consideration.

In the case of a large TR source, we recover the GF equation (2) since the correction term (8) tends to zero for  $a \rightarrow \infty$ .

Formula (11) reveals a frequency dependence of the radiated energy. As stated above, the correction term  $T(\gamma, \omega a, \theta)$  depends on the product  $\omega a \propto a/\lambda$ . This means that the angular distribution remains invariant if the disk radius  $a$  and the wavelength  $\lambda$  of the TR are scaled by the same factor. A simplification of (11) is possible when the argument  $y = \omega a/(c\beta\gamma)$  of the modified Bessel functions is small. Using

$$\lim_{y \rightarrow 0} y K_0(y) = 0, \quad \lim_{y \rightarrow 0} y K_1(y) = 1,$$

we obtain the useful approximation

$$\frac{d^2 U_{\text{disk}}}{d\omega d\Omega} \approx \frac{d^2 U_{\text{GF}}}{d\omega d\Omega} \left[1 - J_0\left(\frac{\omega a \sin\theta}{c}\right)\right]^2. \quad (12)$$

## D. Validity range of the Ginzburg-Frank formula

### 1. Near-field diffraction

In order to cover the near-field case, we use the second-order expansion (5) of the distance  $R'$  between an arbitrary source point  $Q = (\rho, \phi, 0)$  and the observation point  $P = (x, 0, D)$ . Note that  $x/R = \sin\theta$  is usually also much smaller than 1. The angular dependence of the intensity is in second order

$$\frac{d^2 U^{(2)}}{d\omega d\Omega} = C \left| \int_0^a J_1(k\rho \sin\theta) K_1\left(\frac{k\rho}{\beta\gamma}\right) \exp\left(\frac{ik\rho^2}{2R}\right) \rho d\rho \right|^2 \quad (13)$$

with the coefficient  $C = e^2 \omega^4 / (4\pi^3 \epsilon_0 c^5 \beta^4 \gamma^2)$ . The integral (13) is evaluated numerically. It is instructive to compare this to the first-order angular distribution derived in the previous section:

$$\frac{d^2 U^{(1)}}{d\omega d\Omega} = C \left| \int_0^a J_1(k\rho \sin\theta) K_1\left(\frac{k\rho}{\beta\gamma}\right) \rho d\rho \right|^2. \quad (14)$$

Note the similarity between the two integrals: in order to account for near-field diffraction it is sufficient to include the additional phase factor  $\exp[ik\rho^2/(2R)]$ . This fact will be used in the numerical computation of diffraction patterns by fast Fourier transformation. Formula (13) has been very useful for us in designing the basic optical layout of the CTR beamline.

### 2. Effective source radius and far-field condition

The GF angular distribution is valid if the disk radius  $a$  is large and the observation screen sufficiently far away. The question is, how large the radius has to be. Following [31] we define an *effective source radius* by

$$r_{\text{eff}} = \gamma\lambda. \quad (15)$$

The first condition for obtaining the GF angular distribution is that the TR screen radius  $a$  has to exceed the effective source radius

$$a \geq r_{\text{eff}} = \gamma\lambda. \quad (16)$$

When this condition is fulfilled, the term  $T(\gamma, \omega a, \theta)$  in the generalized GF formula (11) is much smaller than 1. If, however, the screen radius  $a$  is small compared to the effective source radius, the correction term  $T(\gamma, \omega a, \theta)$  becomes significant, see Fig. 2.

The condition for far-field diffraction can be written as [31]

$$D > \gamma r_{\text{eff}} = \gamma^2 \lambda. \quad (17)$$

This follows from the Fresnel zone construction in light optics. The radius of the  $n$ th Fresnel zone is given

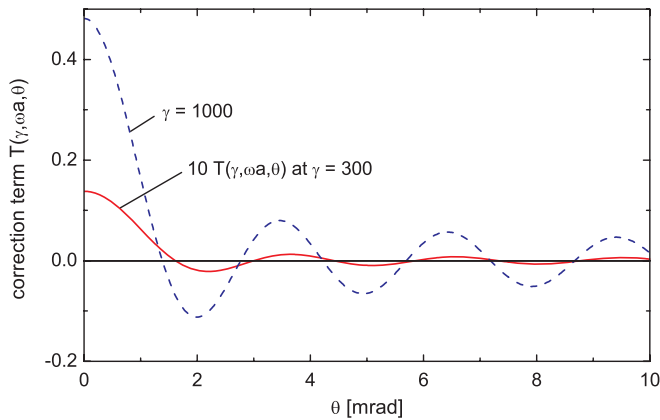


FIG. 2. (Color) The correction term  $T(\gamma, \omega a, \theta)$  in the generalized GF formula (11) is plotted as a function of  $\theta$ . Parameters: frequency  $f = 10$  THz, TR screen radius  $a = 10$  mm. Solid red curve:  $\gamma = 300$ , hence  $a/r_{\text{eff}} = 1.1$ . The effective source-size condition (16) is fulfilled. Plotted here is  $T(\gamma, \omega a, \theta)$  multiplied with a factor of 10, so the correction term is below 1% for  $\theta \geq 1/\gamma$ . Dashed blue curve:  $\gamma = 1000$ ,  $a/r_{\text{eff}} = 0.33$ . Now the effective source-size condition (16) is violated and  $T(\gamma, \omega a, \theta)$  reaches 50% at  $\theta = 0$ .

by  $r_n = \sqrt{n\lambda D}$ . The far field is safely reached when only the first Fresnel zone contributes, i.e., when

$$r_1^2 > r_{\text{eff}}^2 \Rightarrow D > \gamma^2 \lambda.$$

First we study the source-radius condition in the far field for  $\lambda = 0.3$  mm,  $\gamma = 100$ , and  $r_{\text{eff}} = \gamma\lambda = 30$  mm. The far-field condition (17) requires then  $D > 3$  m, we choose  $D = 4$  m. For a source radius  $a \geq r_{\text{eff}}$  both the first-order and the second-order formulas (14) and (13) are found to be in perfect agreement with the GF formula. However, for

a very small source radius, e.g.  $a = 0.1 \cdot r_{\text{eff}}$ , the angular distribution becomes much wider than predicted by GF, as can be seen in the left part of Fig. 3. It is interesting to note that in the far-field regime the first-order equation (14) and the second-order equation (13) yield the same result but both differ considerably from the GF distribution if condition (16) is violated.

Next we choose a screen radius equal to the effective source radius, but consider the extreme near-field case with  $D = 0.2$  m. In the right part of Fig. 3 the first-order and second-order angular distributions are compared to the GF angular distribution. The first-order equation (14) is in perfect agreement with the GF formula but the correct second-order formula (13) yields a significantly wider distribution. This is clear evidence for a near-field effect. An important result of our investigations is that there is no need to go to even higher orders in the Taylor expansion of  $R'$ . The results obtained with the second-order formula (13) are, for all cases considered, in good agreement with a two-dimensional numerical computation based on the exact square-root expression (5) for the distance  $R'$ .

### III. DESCRIPTION OF THE CTR BEAMLINE

#### A. Design criteria

The CTR beamline at FLASH is installed in the straight section between linac and undulator. Its purpose is to transport transition or diffraction radiation with high efficiency over a distance of 18.7 m to an experimental laboratory outside the tunnel. To obtain a very large bandwidth from a few 100 GHz up to optical frequencies, a diamond window is used to couple the radiation from the ultrahigh vacuum (UHV) chamber of the electron linac into the CTR beamline, diamond being the only material with high trans-

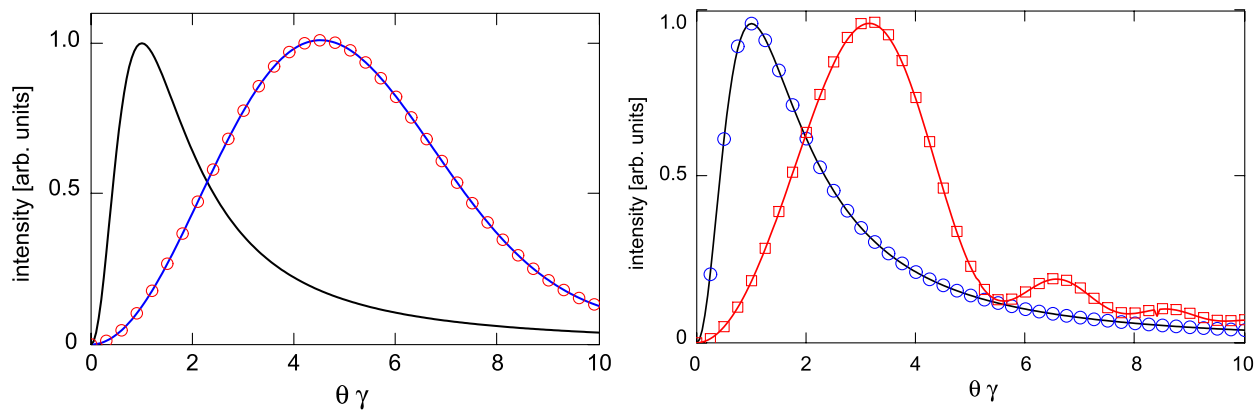


FIG. 3. (Color) Left: Far-field TR from a circular disk for  $\lambda = 0.3$  mm,  $\gamma = 100$ ,  $r_{\text{eff}} = 30$  mm,  $D = 4$  m. The far-field condition (17) is satisfied:  $D > \gamma r_{\text{eff}} = 3$  m. The TR source radius is  $a = 0.1 \cdot r_{\text{eff}}$ , so the source-size condition (16) is strongly violated. Black curve: GF formula; blue curve: first-order computation using Eq. (14); red circles: second-order computation using Eq. (13). The distributions are individually normalized to a maximum value of 1. Right: Near-field TR from a circular disk for  $\lambda = 0.3$  mm,  $\gamma = 100$ ,  $a = r_{\text{eff}} = 30$  mm,  $D = 0.2$  m. The effective source-size condition (16) is fulfilled but the far-field condition (17) is badly violated. Black curve: GF formula; blue circles: first-order computation using Eq. (14); red curve: second-order calculation using Eq. (13); red squares: numerical calculation using the exact square-root expression for  $R'$ .

mission in this entire frequency range. The beamline is evacuated to better than 0.1 mbar to suppress the water vapor absorption lines which would strongly distort the frequency spectrum in a transfer channel filled with air of normal humidity. The focusing of the THz beam is done with concave mirrors because lenses made from any material other than diamond would absorb most THz radiation above 4 THz. In the design of the beamline optics, special attention must be paid to the low-frequency range because here the beam suffers appreciable widening by diffraction. A major constraint in this respect is a 9 m long tube of 200 mm diameter through which the radiation has to be guided to cross the shielding wall of the accelerator. No focusing mirrors can be used inside this tube.

### B. Vacuum window at the linac beam pipe

Conventional window materials for THz applications are low-density polyethylene (LDPE) and single-crystal quartz, but by far the best choice is chemical vapor deposition (CVD) diamond [38]. In Fig. 4 the transmission coefficients of the three window materials are plotted as a function of wavelength. The intensity transmission coefficient  $T(\lambda)$  has been calculated as a function of wavelength from measured data on the refractive index  $n(\lambda)$  and the extinction coefficient  $\kappa(\lambda)$ , reported for diamond in Ref. [38] and for crystalline quartz and low-density polyethylene in Ref. [39].

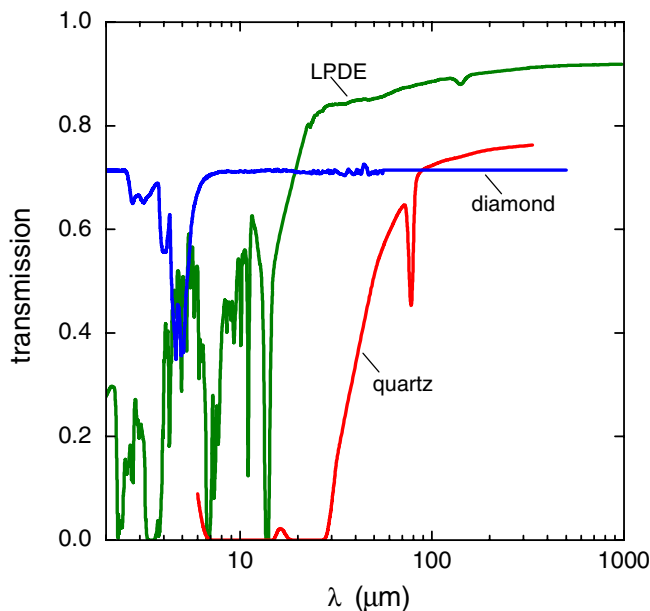


FIG. 4. (Color) Intensity transmission coefficient as a function of wavelength for a 0.5 mm thick window made from CVD diamond, low-density polyethylene LDPE or single-crystal quartz. The transmission coefficient of the diamond window is 71% because of reflection losses, except in the region between 2 and 7  $\mu\text{m}$  where absorption occurs due to the excitation of lattice vibrations.

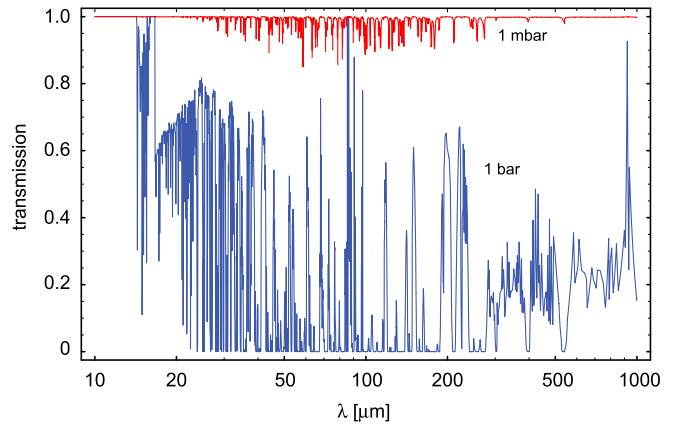


FIG. 5. (Color) Transmission through 20 m of air with 50% relative humidity as a function of wavelength. The pressure is 1 bar (blue), respectively 1 mbar (red).

### C. Absorption of THz radiation in humid air

Air with normal humidity has a high absorption for THz radiation [40] as can be seen from Fig. 5. To obtain a wavelength-independent transfer efficiency, the beamline needs to be evacuated to a pressure of less than 0.1 mbar.

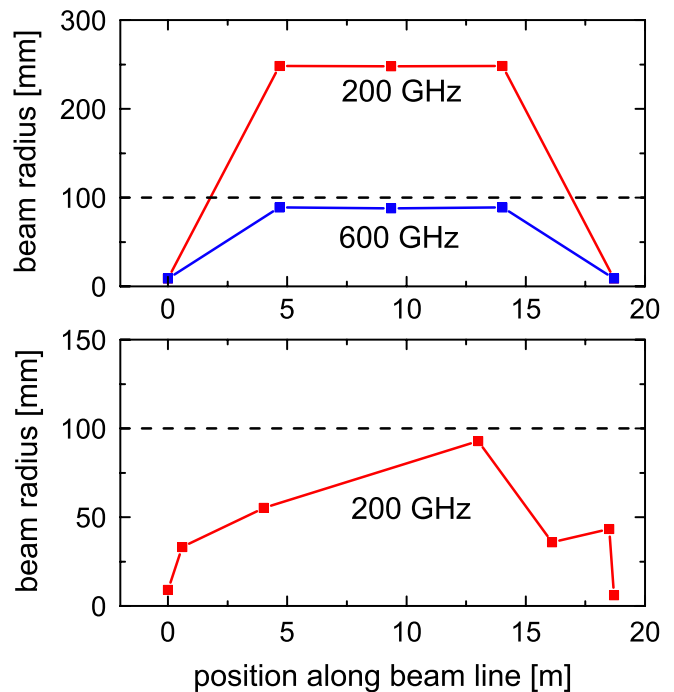


FIG. 6. (Color) Top graph: Transport of a Gaussian beam with frequency  $f = 200$  GHz (red squares), respectively  $f = 600$  GHz (blue squares), through a beamline of length  $D = 18.7$  m. The focusing is provided by two lenses of focal length  $f_1 = f_2 = D/4$ , which are placed at the positions  $z_1 = D/4$  and  $z_2 = 3D/4$ . The initial waist radius is  $w_0 = 9$  mm. The envelope of the beam is sketched. The radius of the beam pipe of 100 mm is indicated by the dash-dotted line. Bottom graph: Transport of a 200 GHz Gaussian beam through a five-lens arrangement according to Fig. 7.

### D. Optical layout of the beamline

The transport of a Gaussian laser beam over a distance  $D$  is conveniently done with two lenses of focal length  $f_1 = f_2 = D/4$ , which are placed at the positions  $z_1 = D/4$  and  $z_2 = 3D/4$ . The transfer matrix of this system is the negative unit matrix, so a beam waist at the laser output is imaged to a waist of the same size at the observation plane  $z = D$ . The boundary conditions at the FLASH linac require a deviation from this ideal optical setup because it is not possible to install focusing mirrors in the 9 m long tube inside the shielding wall. More importantly, in order to cope with the strong diffractive beam widening at frequencies below 1 THz, the first focusing element of the transfer line has to be positioned much closer to the radiation screen than  $z_1 = D/4 = 4.7$  m, because otherwise the beam tube would strongly suppress the low-frequency components. This is demonstrated in Fig. 6, where the envelope of a Gaussian beam is plotted schematically for a frequency  $f = 200$  GHz and an initial beam waist radius  $w_0 = 9$  mm. One can see that the beam radius exceeds the tube radius of 100 mm by more than a factor of 2. For this reason more than two focusing elements are needed. A beam line with five focusing elements reduces the maximum radius of the 200 GHz Gaussian beam to less than 100 mm. A schematic view of the beamline optics is shown in Fig. 7.

### E. Technical layout of the CTR beamline

The main components of the CTR source and beamline are: a special UHV chamber in the linac containing four movable transition and diffraction radiation screens, a diamond exit window, an evacuated transfer channel equipped with five focusing mirrors F1 to F5 and four plane mirrors P1 to P4. The arrangement of the mirrors is shown in Fig. 8. The final component is a large vacuum vessel for carrying out interferometric, spectroscopic, or electro-optic experiments utilizing the full THz spectrum. For experiments to be carried out in air, the radiation can be coupled out of the beamline through a window (quartz, NaCl, LDPE), however at the price of a restricted frequency range.

A MATHEMATICA code *THzTransport* has been developed in order to compute the generation of transition radiation from a screen of arbitrary size and shape and to

transport the radiation through the beamline. For the propagation of electromagnetic radiation from one optical element of the beamline to the next element, the code employs the Fourier transform method based on the physical optics approach (see Refs. [37,41,42]). The same method is applied in the commercially available code ZEMAX [43] and in the code SRW developed at the ESRF [44].

The optical performance of the beamline for transition radiation at 200 GHz is demonstrated in Fig. 8. Here the  $45^\circ$  inclination angle of the TR screen with respect to the electron beam has been taken into account as well as the multiple reflections in the wedge-shaped diamond window (see below). The code *THzTransport* was used to compute the two-dimensional intensity distributions at the window and the five focusing elements. From this figure it is obvious that the focusing mirror F3 with a diameter of 190 mm constitutes the tightest aperture limitation at low frequency. A sizable fraction of the 200 GHz beam is not accepted by this aperture.

The beam line was installed in August 2005 and is presently being used for bunch diagnostics with coherent transition radiation spectroscopy.

#### 1. Diamond window

Since the price of CVD diamond windows increases very rapidly with size, it was decided to use a small window with a radius  $r_w = 10$  mm and place it at the closest technically feasible distance to the TR screen. This minimum distance is 40 mm. The refractive index of CVD diamond is  $n_0 = 2.38$  for wavelengths above  $10 \mu\text{m}$  [38]. We first consider a diamond slab of thickness  $d_0$  with plane-parallel faces. At the front, respectively rear, surface of the diamond slab, an incident THz wave is partly transmitted and partly reflected. The transmitted THz energy, summed over the multiple reflections at the front and rear surface of the window and normalized to the incident energy, is found to be [37]

$$\frac{U_{\text{trans}}}{U_0} = \frac{8n_0^2}{n_0^4 + 6n_0^2 + 1 - (n_0^2 - 1)^2 \cos(2n_0kd_0)}. \quad (18)$$

This energy transmission ratio is depicted in Fig. 9 as a function of frequency. It exhibits strong oscillations between 50% and 100%, which can be suppressed by using a window of nonuniform thickness. It is technically feasible

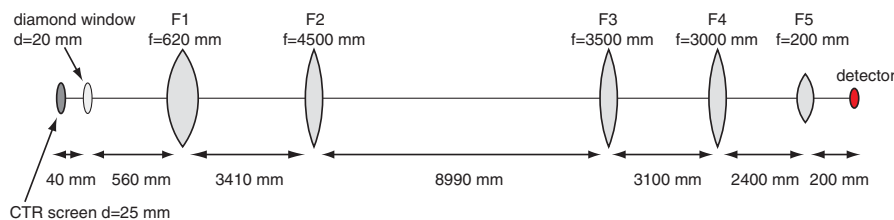


FIG. 7. Schematic optical design of the THz transfer line. The focusing elements F1 to F5 are shown as lenses with their respective positions and focal lengths.

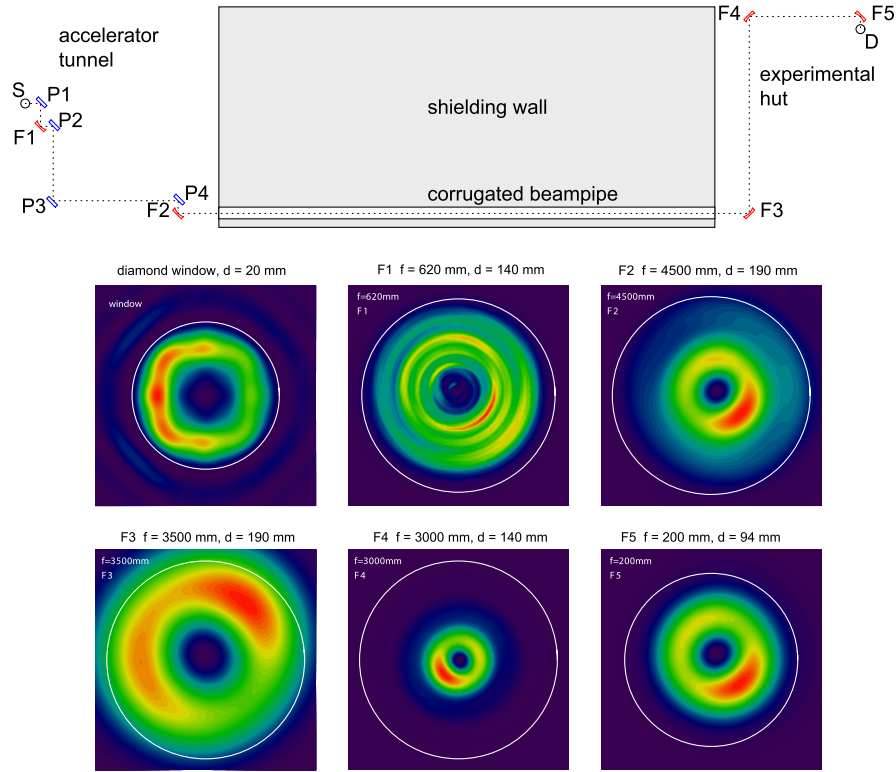


FIG. 8. (Color) Top: Layout of the CTR beamline with transition radiation screen S, five focusing mirrors F1 to F5, four plane mirrors P1 to P4, and detector D. The sketch is somewhat simplified. In reality, the optical path between the mirrors F1 and P2 and between F4 and F5 is perpendicular to the plane of the drawing. Thereby the polarization of the radiation is rotated by 90°. Middle and bottom row: The two-dimensional intensity distributions at the diamond window and the five focusing mirrors F1 to F5. The circles indicate the free aperture of each optical element. The diameters  $d$  are listed on top of the pictures. The deviations from cylindrical symmetry are mainly caused by the rectangular shape and 45° tilt angle of the TR screen, and by the wedge-shaped diamond window. The wedge direction is oriented at 45° with respect to the horizontal axis. The generation and propagation of transition radiation with a frequency  $f = 200$  GHz has been modeled using the program *THzTransport*. The Lorentz factor of the electrons is  $\gamma = 1000$ .

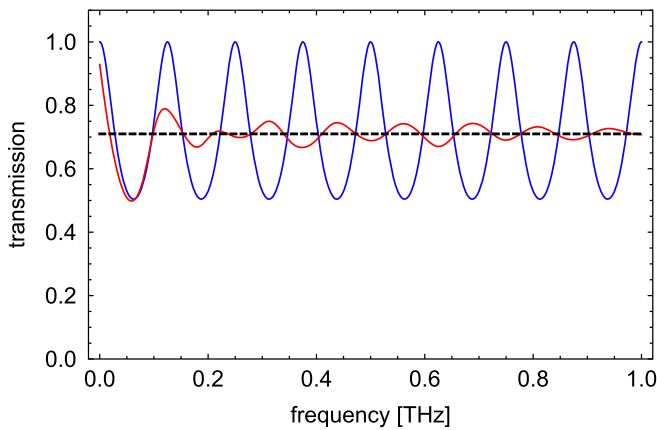


FIG. 9. (Color) Ratio of transmitted to incident energy as a function of frequency. The blue curve applies for a plane-parallel CVD diamond window with a thickness of  $d_0 = 0.5$  mm, while the red curve refers to a wedge-shaped window with a wedge angle  $\alpha_w = 1^\circ$ . The average energy transmission ratio is 0.71 in both cases (dashed black line). Note that the 29% energy reduction is entirely due to reflection losses at the front and rear surface.

to grind a CVD diamond window with a wedge angle  $\alpha_w = 1^\circ$ . The computed energy transmission ratio for such a window is also shown Fig. 9. The average energy transmission ratio is 0.71. Beyond 1 THz the transmission becomes almost independent of frequency.

The window of the CTR beamline has been produced with this wedge angle of  $1^\circ$ . The window acts as a prism with a deflection angle of  $(n_0 - 1)\alpha_w$ .

Note that in case of linearly polarized radiation the reflections at the surface can be eliminated if the window is tilted by the Brewster angle. This is unfortunately impossible for the radially polarized transition radiation.

## 2. Screens for the generation of transition and diffraction radiation

The size of the TR screen is constrained by the small aperture of the diamond window. The window has a radius of  $r_w = 10$  mm and is placed at a distance of 40 mm from the electron beam. For  $\gamma = 1000$  and a frequency of 200 GHz, we have calculated the TR intensity at the window for a circular TR screen with a radius  $a$  varying

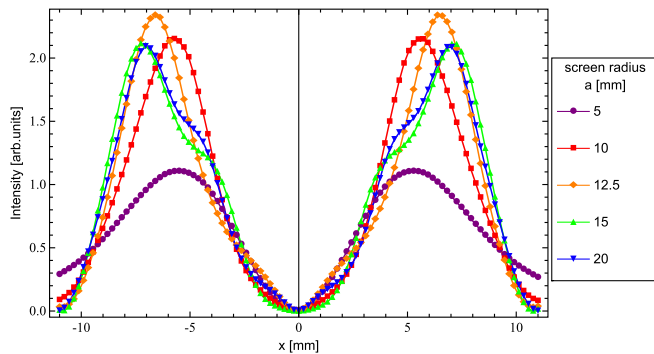


FIG. 10. (Color) Horizontal intensity distribution of 200 GHz transition radiation on the diamond window. The TR screen radius  $a$  is varied between 5 and 20 mm.

between 5 and 20 mm. For simplicity, the calculations have been done for backward transition radiation. The results are presented in Fig. 10. From this figure, the best choice for the TR screen radius appears to be  $a = 12.5$  mm. In reality the screen has an inclination angle of  $45^\circ$  with respect to the electron beam direction, so ideally it should have an elliptical shape with a short half axis of 12.5 mm and a long half axis of 17 mm to appear as a circle to the incident beam. For technical reasons the TR screens have been fabricated with a rectangular shape.

Four different screens are installed to produce coherent radiation for beam diagnostics: (i) a full screen for transition radiation with a size of  $36 \times 25$  mm<sup>2</sup> that appears to the incident electron beam as a square of 25 mm side length; (ii) an off-axis TR screen with a size of  $16 \times 25$  mm<sup>2</sup> which is positioned outside the electron beam; (iii) a diffraction radiation screen with a central hole of 2 mm radius to permit beam diagnostics with a long train of electron bunches during FEL operation; and (iv) a slit-type diffraction radiator with 4 mm slit width.

The screens are made from  $380 \mu\text{m}$  thick polished silicon wafers and coated with a 150 nm aluminum layer. The off-axis TR screen serves as a transition radiator by steering selected electron bunches onto this screen using a kicker magnet. This screen is particularly valuable as it permits high-resolution diagnostics on a single bunch out of a long train without impeding the FEL gain process for the unkicked bunches.

### 3. Suppression of waveguide modes in the pipe

The vacuum tube of the CTR beamline is made from stainless steel. The diameter was chosen as large as possible taking into account the boundary conditions at the accelerator. The most critical part is the 9 m long section inside the shielding wall of the linac where the diameter of the pipe is restricted to 200 mm. At the end of this section the outer rim of a low-frequency THz beam ( $f \leq 300$  GHz) hits the beam tube. An important design goal was to prevent reflections at the metallic wall because these

TABLE I. Focal lengths and diameters (as seen by the incident beam) of the focusing mirrors in the CTR beamline.

Mirror	F1	F2	F3	F4	F5
Focal length [mm]	620	4500	3500	3000	200
Diameter [mm]	140	190	190	140	94

could easily destroy the narrow time profile of the THz pulse. The first idea was to cover the tube wall with a microwave-absorbing material; however, it turned out impossible to find a material with a high absorption at glancing incidence angles and in a broad frequency band from 200 GHz to 100 THz, which moreover was suitable for vacuum.

An elegant alternative solution was found: using a stainless steel bellows instead of a tube with a smooth wall, all electromagnetic waves with a wavelength significantly shorter than the corrugation length undergo chaotic scattering at the wall of the bellows and are thereby prohibited from propagating in a waveguide mode. This idea was experimentally verified with infrared light from a laser diode and with thermal radiation from a heated source.

### 4. Mirrors

All mirrors in the CTR beamline deflect the beam by  $90^\circ$ . They have an elliptical outer contour to appear as circular apertures when viewed along the beam direction. The focusing mirrors F1 to F4 are toroids with a ratio of radii of 1:2. The focal lengths and the dimensions are listed in Table I. These mirrors were manufactured by the company LT Ultra-Precision Technology from massive steel, respectively aluminum-alloy, plates with precision diamond tooling. The specified surface roughness is  $R_a \leq 10$  nm, the average deviation from the ideal surface contour is  $\leq 0.5 \mu\text{m}$  in the center region of the mirrors and  $\leq 5 \mu\text{m}$  near the rim. Mirror F5 is an off-axis paraboloid and was manufactured by Kugler Precision. All mirrors are hard plated with gold and feature a very high reflectivity in the THz and infrared regime. The specified values at  $10.6 \mu\text{m}$  and  $45^\circ$  incidence angle are 99.4% for  $S$  polarization and 98.5% for  $P$  polarization. The micromovers of the mirrors F1, F2, F3, F4, and P3 are equipped with stepping motors to facilitate remotely controlled optical alignment of the beamline in the evacuated state. The alignment of the mirrors has been performed using a red laser and optical transition radiation.

### F. Energy transmission of the CTR beamline

An important aim in designing the CTR beamline was to obtain a large transmission efficiency for electromagnetic radiation over a wide frequency range. We consider first the aperture limitations given by the diamond window and the first focusing mirror F1, and compute then the spectral energy which is to be expected at the end of the beamline.

### 1. Geometric acceptance of diamond window and mirror F1

The diamond window constitutes the first aperture of the CTR beamline. The question is whether the small size of this window determines the angular acceptance of the beamline. In order to investigate this question semianalytically, we consider first the simplified case of backward TR. The influence of the  $45^\circ$  inclination angle of the TR screen and its rectangular shape are studied in the next section. The acceptance angle of the window is  $\theta_w = \arctan(r_w/D_w) = 14^\circ$ , where  $r_w = 10$  mm is the radius of the window and  $D_w = 40$  mm its distance from the radiation screen. The window aperture is in the near-field region; hence, we use the second-order formula (13) and integrate it numerically over the acceptance angle of the window. The fraction of TR energy within this solid angle is

$$\eta_w = \left[ \int_0^{\theta_w} \frac{d^2 U^{(2)}}{d\omega d\Omega} \sin\theta d\theta \right] \left[ \int_0^{\pi/2} \frac{d^2 U^{(2)}}{d\omega d\Omega} \sin\theta d\theta \right]^{-1}. \quad (19)$$

The same procedure is applied for the first plane mirror P1 (radius 27 mm, distance 240 mm from the TR screen) and the first focusing mirror F1 (radius 70 mm, distance 600 mm). The geometric acceptances are shown in Fig. 11 as functions of frequency. From this figure it is obvious that the mirror F1 has a smaller geometric acceptance than the diamond window. The size of the plane mirror P1 was intentionally chosen to match the acceptance of F1. The conclusion is that an enlargement of the

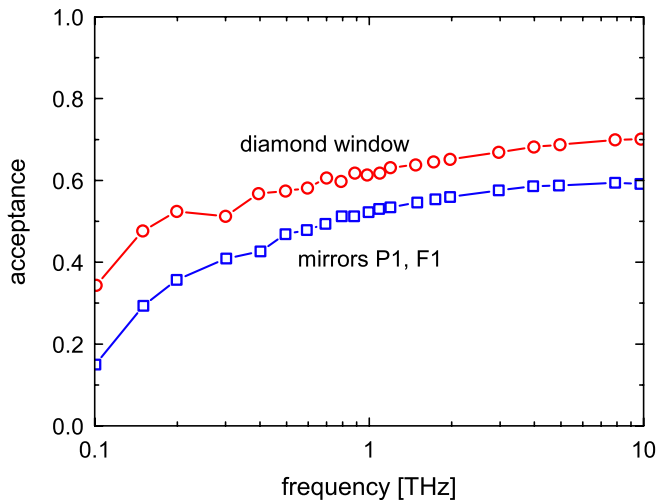


FIG. 11. (Color) Frequency-dependent acceptance of the diamond window (red curve and circles), respectively the mirrors P1 (blue squares) and F1 (blue curve), for transition radiation from a circular screen of radius  $a = 12.5$  mm. The plateau values of about 70% for the window and 60% for the mirrors P1, respectively F1, are reached at frequencies above 5 THz. It is obvious that the mirrors constitute a tighter acceptance limitation than the diamond window.

window would not improve the overall acceptance of the CTR beamline. The remaining mirrors in the beamline are matched in size to F1 and cause no further losses for frequencies above 1 THz. At lower frequencies, however, the beam widens considerably by diffraction when passing through the beamline, and then the limitation is given by the mirror F3 which is located behind the 9 m long tube crossing the shielding wall of the accelerator (compare Figs. 7 and 8).

It is interesting to note that the aperture limitation caused by the mirror F1 is even effective at optical frequencies where the wavelengths are many orders of magnitude smaller than the mirror dimensions. The reason is the wide tail in the angular distribution of transition radiation. In that respect optical transition radiation is very different from laser light.

### 2. Transmission of beamline as a function of frequency

The code *THzTransport* has been used to compute the propagation of TR through the actual beamline. In Fig. 12 we show the computed ratio  $U_{\text{fin}}/U_{\text{P1}}$  as a function of frequency, where  $U_{\text{fin}}$  is the spectral energy density at the final focus of the beamline and  $U_{\text{P1}}$  the spectral energy density at the first mirror P1 behind the diamond window. This ratio is small at frequencies below 300 GHz, owing to diffraction losses in the beamline, but rises steeply to a plateau of about 90%.

### 3. Estimation of CTR spectral energy

The longitudinally compressed electron bunches in FLASH are characterized by a short leading spike containing 10%–20% of the bunch charge and a long tail. In our model calculation, we approximate the leading spike by a Gaussian width  $\sigma_t = 15$  fs and a charge of 0.1 nC (number

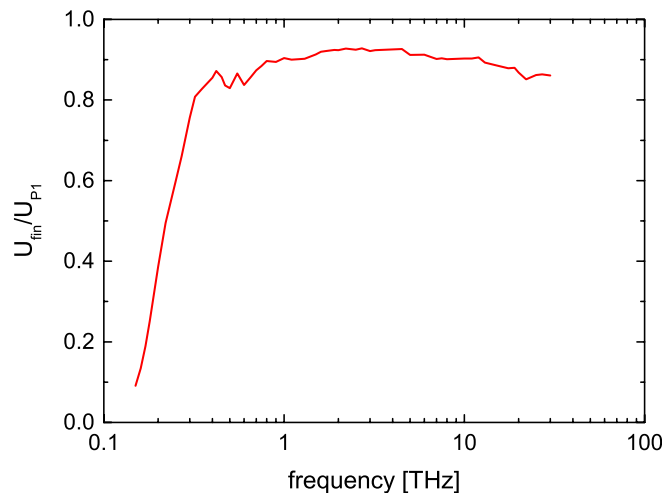


FIG. 12. (Color) The ratio  $U_{\text{fin}}/U_{\text{P1}}$  as a function of frequency. Here  $U_{\text{fin}}$  is the spectral energy density at the final focus of the beamline and  $U_{\text{P1}}$  the spectral energy density at the first mirror P1 behind the diamond window.

of electrons  $N_e = 0.62 \times 10^9$ ). The tail is disregarded here. The longitudinal form factor is

$$F_{\text{long}}(\omega) = \exp(-\sigma_t^2 \omega^2 / 2). \quad (20)$$

The finite beam radius is taken into consideration assuming a simple transverse charge distribution, namely, a cylindrical electron bunch of radius  $r_b$  with homogeneous charge density. The Fourier-transformed radial electric field is

$$\tilde{E}_r(\rho, \omega) = C_1(\omega) \begin{cases} K_1\left(\frac{\omega r_b}{c\beta\gamma}\right) I_1\left(\frac{\omega \rho}{c\beta\gamma}\right) & \text{for } \rho < r_b \\ I_1\left(\frac{\omega r_b}{c\beta\gamma}\right) K_1\left(\frac{\omega \rho}{c\beta\gamma}\right) & \text{for } \rho > r_b \end{cases} \quad (21)$$

with the coefficient function

$$C_1(\omega) = \frac{-2eN_e F_{\text{long}}(\omega)}{(2\pi)^{3/2} c\beta\epsilon_0 r_b}.$$

The presence of the cylindrical electron beam pipe requires to add a second term of the form

$$C_2 I_1\left(\frac{\omega \rho}{c\beta\gamma}\right)$$

with a coefficient  $C_2$  that depends on the frequency  $\omega$ , the bunch radius  $r_b$ , the pipe radius  $r_p$ , and the resistivity of the pipe, for details see e.g. [45]. For our rather large pipe radius of  $r_p = 30$  mm this term is insignificant in comparison with the correction term (8) introduced by the finite TR screen radius, so we neglect it here. Following the procedure outlined in Sec. II, the CTR spectral density is found to be [37]

$$\frac{d^2 U_{\text{bunch}}}{d\omega d\Omega} = \frac{d^2 U_{\text{GF}}}{d\omega d\Omega} \cdot N_e^2 |F_{\text{long}}(\omega)|^2 \times \left[ \frac{2J_1(x)}{x} - \frac{2I_1(y)}{y} T(\gamma, \omega a, \theta) \right]^2 \quad (22)$$

with  $x = \frac{\omega r_b \sin\theta}{c}$ ,  $y = \frac{\omega r_b}{c\beta\gamma}$ .

This formula is valid in the far field.

We note that in the limit of a very thin and very short bunch ( $r_b \rightarrow 0$  and  $F_{\text{long}}(\omega) \rightarrow 1$ ), the expression (22) reduces to the generalized GF equation (11), applied to a bunch of  $N_e$  electrons, since  $2J_1(x) \approx x$  and  $2I_1(y) \approx y$  for small arguments. An important observation is that the bunch radius enters in the form  $r_b \sin\theta \ll r_b$ . Therefore, the radial dimension of the bunch will have a rather weak influence on the CTR frequency spectrum and is in fact of minor importance for the finely collimated beam at FLASH ( $r_b \approx 100 \mu\text{m}$ ).

In order to estimate the CTR spectral energy that can be expected at FLASH, we consider the leading spike of the compressed electron bunch and use the Fourier-transform method in the near-field approximation to propagate the CTR pulse stepwise through the actual beamline. The computed spectrum of the CTR pulse having passed the entire beamline is shown in Fig. 13. The spectral energy at

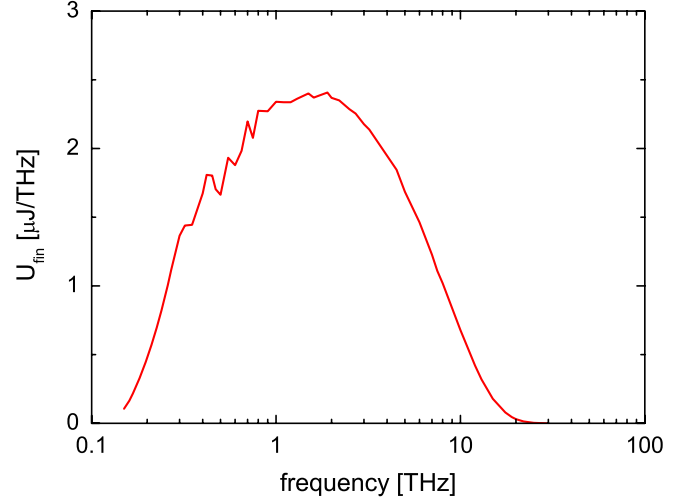


FIG. 13. (Color) Computed spectral CTR pulse energy density in  $\mu\text{J}/\text{THz}$  from a 0.1 nC bunch of 15 fs rms length at the final focus of the beamline, plotted as a function of frequency. The Lorentz factor is  $\gamma = 1000$ . The structure in the curve is caused by diffraction effects at the diamond window. The influence of the finite electron beam radius is included.

the focus of the beamline is very small at low frequency ( $f < 300$  GHz), for two reasons: the effective source-size condition is violated, leading to a widening of the TR angular distribution, and diffraction losses in the beamline are significant. The spectral energy rises steeply to a value of more than  $2 \mu\text{J}/\text{THz}$  in the range 0.7–4 THz. Above 5 THz a drop is observed which is mainly caused by the longitudinal form factor of the bunch while the transverse beam dimension has only a minor impact [37].

Figure 13 demonstrates convincingly that coherent transition radiation in combination with the CTR beamline at FLASH can indeed be utilized as a THz source of high pulse energy ( $> 10 \mu\text{J}$ ) and very large bandwidth (0.2–20 THz). If the bunch possesses substructures with time scales below 15 fs, the CTR spectrum will even extend beyond 20 THz. There is experimental evidence for this, see Sec. IV.

#### IV. EXPERIMENTAL RESULTS

To illustrate the performance of the CTR source and beamline we give here a very brief description of some of the beam diagnostic experiments carried out at the beamline. The experiments are still ongoing.

Since the CTR spectrum was expected to cover more than two decades in wavelength, a broadband infrared spectrometer was developed which is mounted in a vacuum vessel attached to the CTR beamline. The radiation is dispersed by a sequence of reflecting blazed gratings and recorded by line arrays of pyroelectric detectors with fast readout. Using this spectrometer the coherent radiation spectrum of the compressed electron bunches used for FEL light production was determined in the wavelength

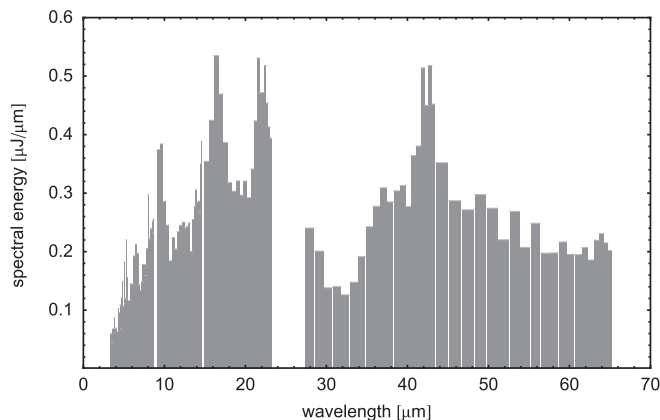


FIG. 14. Spectral energy  $dU/d\lambda$  of coherent transition radiation from longitudinally compressed electron bunches, recorded during normal FEL-mode operation (preliminary data). Six different gratings were used to subdivide the wavelength range from 3 to 65  $\mu\text{m}$ .

range from 3 to 300  $\mu\text{m}$  (frequency range 1–100 THz) [46].

In recent measurements with a pyroelectric detector array which was calibrated at the infrared free-electron laser FELIX in the Netherlands, surprisingly large CTR intensities in the near-infrared regime have been observed [47]. Preliminary data ranging from 3 to 65  $\mu\text{m}$  are shown in Fig. 14. There is an overall normalization uncertainty of about 30% due to calibration uncertainties of the infrared

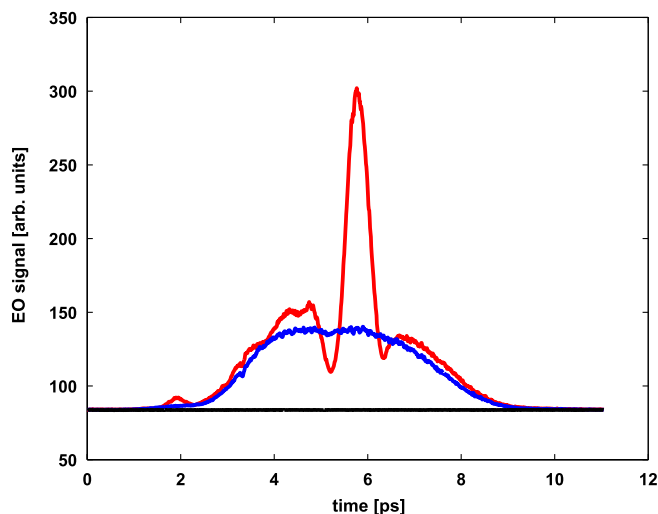


FIG. 15. (Color) A single-shot electro-optic (EO) measurement of the CTR pulse emitted by a compressed electron bunch in the FLASH linac. The EO spectral decoding technique [52] was applied. A 175  $\mu\text{m}$  thick gallium-phosphide crystal was placed in the focal plane of the beamline, and the induced birefringence was retrieved with a chirped titanium-sapphire laser pulse. Red curve: EO signal with CTR pulse present; blue curve: background without CTR pulse; black line: background noise in CCD camera image.

power meters available at FELIX, but the relative calibration of the different spectrometers channels is accurate to better than 10%. The total CTR pulse energy in the wavelength range 3 to 65  $\mu\text{m}$  (frequency range 5 to 100 THz) is in the order of 10  $\mu\text{J}$ .

The rather large radiation energy in the near infrared is clear experimental evidence for the microbunching effects that have been predicted to happen in magnetic bunch compressor chicanes (see, e.g., Refs. [48–50], and the literature quoted therein). These highly interesting measurements are being continued and will be reported elsewhere.

The CTR beamline preserves the narrow pulse shape of CTR pulses that are emitted by ultrashort electron bunches. This property was demonstrated using an electro-optic (EO) detector in the focal plane of the beamline [51]. A recent single-shot measurement made with a new EO setup is presented in Fig. 15. An impressive EO signal is observed. The CTR beamline is well suited to characterize new electro-optic materials as it offers high THz intensity over a wide frequency range from 200 GHz up to about 100 THz.

## V. SUMMARY

We have designed and implemented a transition radiation source and a beamline transporting the radiation to a laboratory outside the accelerator tunnel of FLASH. The design was based on detailed theoretical studies on the generation and propagation of transition radiation. A MATHEMATICA code *THzTransport* was developed to generate transition radiation on screens of arbitrary size and shape and to propagate the radiation from one optical element of the beamline to the next element by fast Fourier transformation. A specific design goal of the CTR beamline was to achieve high transmission from about 200 GHz up to optical frequencies and to preserve narrow pulse shapes. Recent experimental results on the spectroscopy of coherent transition radiation and the electro-optic detection of ultrashort THz pulses demonstrate that the CTR source and beamline perform according to expectations. Pulse energies of more than 10  $\mu\text{J}$  have been observed in a frequency band from 200 GHz to about 100 THz.

## ACKNOWLEDGMENTS

We gratefully acknowledge the help of our engineers and technicians M. Böttcher, J. Hauschildt, K. Ludwig, and O. Peters in constructing the CTR beamline.

- 
- [1] U. Happek, A. J. Sievers, and E. B. Blum, *Phys. Rev. Lett.* **67**, 2962 (1991).
  - [2] Y. Shibata *et al.*, *Phys. Rev. A* **45**, R8340 (1992).

- [3] R. Lai, U. Happek, and A.J. Sievers, Phys. Rev. E **50**, R4294 (1994).
- [4] Y. Shibata *et al.*, Phys. Rev. E **49**, 785 (1994).
- [5] Y. Shibata *et al.*, Phys. Rev. E **50**, 1479 (1994).
- [6] M.S. Zolotarev and K.T. McDonald, <http://www.hep.princeton.edu/~mcdonald/accel/weizsacker.pdf>.
- [7] P. Kung *et al.*, Phys. Rev. Lett. **73**, 967 (1994).
- [8] H. Lihn *et al.*, Phys. Rev. E **53**, 6413 (1996).
- [9] M. Ding, H.H. Weits, and D. Oepts, Nucl. Instrum. Methods Phys. Res., Sect. A **393**, 504 (1997).
- [10] A. Murokh *et al.*, Nucl. Instrum. Methods Phys. Res., Sect. A **410**, 452 (1998).
- [11] M. Geitz *et al.*, Nucl. Instrum. Methods Phys. Res., Sect. A **445**, 343 (2000).
- [12] A. Winter *et al.*, in *Proceedings of the 9th European Particle Accelerator Conference, Lucerne, 2004* (EPS-AG, Lucerne, 2004).
- [13] C.S. Thongbai and T. Vilaithong, Nucl. Instrum. Methods Phys. Res., Sect. A **581**, 874 (2007).
- [14] See <http://infrared.als.lbl.gov/content/web-links/45-srir> or <http://www.lightsources.org>.
- [15] W.R. McKinney *et al.*, Proc. SPIE Int. Soc. Opt. Eng. **3775**, 37 (1999).
- [16] R.P.S.M. Lobo *et al.*, Rev. Sci. Instrum. **70**, 2899 (1999).
- [17] U. Schade *et al.*, Rev. Sci. Instrum. **73**, 1568 (2002).
- [18] T.E. May, R.A. Bosch, and R.L. Julian, in *Proceedings of the 18th Particle Accelerator Conference, New York, 1999* (IEEE, New York, 1999), p. 2394.
- [19] Y.-L. Mathis, B. Gasharova, and D. Moss, J. Biol. Phys. **29**, 313 (2003).
- [20] P. Dumas *et al.*, Infrared Phys. Technol. **49**, 152 (2006).
- [21] T. May, T. Ellis, and R. Reininger, Nucl. Instrum. Methods Phys. Res., Sect. A **582**, 111 (2007).
- [22] J.M. Klopff *et al.*, Nucl. Instrum. Methods Phys. Res., Sect. A **582**, 114 (2007).
- [23] E. Karantzoulis *et al.*, in *Proceedings of the 11th European Particle Accelerator Conference, Genoa, 2008* (EPS-AG, Genoa, Italy, 2008).
- [24] W. Seidel *et al.*, Proceedings of FEL07, Novosibirsk (2007).
- [25] M. Gensch *et al.*, Infrared Phys. Technol. **51**, 423 (2008).
- [26] A.F.G. van der Meer, Nucl. Instrum. Methods Phys. Res., Sect. B **528**, 8 (2004).
- [27] M. Abo-Bakr *et al.*, Phys. Rev. Lett. **88**, 254801 (2002); **90**, 094801 (2003).
- [28] A.-S. Müller *et al.*, in *Proceedings of the 21st Particle Accelerator Conference, Knoxville, 2005* (IEEE, Piscataway, NJ, 2005), p. 2409.
- [29] G.L. Carr *et al.*, Nature (London) **420**, 153 (2002).
- [30] V.A. Verzilov, Phys. Lett. A **273**, 135 (2000).
- [31] M. Castellano *et al.*, Nucl. Instrum. Methods Phys. Res., Sect. A **435**, 297 (1999).
- [32] L.D. Landau and E.M. Lifshitz, *Electrodynamics of Continuous Media* (Pergamon Press, New York, 1960).
- [33] M.L. Ter-Mikaelian, *High-Energy Electromagnetic Processes in Condensed Media* (Wiley-Interscience, New York, 1972).
- [34] B.M. Bolotovskii and E.A. Galst'yan, Phys. Usp. **43**, 755 (2000).
- [35] J.D. Jackson, *Classical Electrodynamics* (John Wiley & Sons, New York, 1998), 3rd ed.
- [36] D. Sütterlin *et al.*, Nucl. Instrum. Methods Phys. Res., Sect. B **264**, 361 (2007).
- [37] S. Casalbuoni, B. Schmidt, and P. Schmüser, DESY TESLA Report No. 2005-015, 2005.
- [38] P. Dore *et al.*, Appl. Opt. **37**, 5731 (1998).
- [39] E. Palik, *Handbook of Optical Constants of Solids* (Academic Press, New York, 1985).
- [40] P.U. Jepsen (private communication).
- [41] J.W. Goodman, *Introduction to Fourier Optics* (McGraw-Hill, New York, 1968).
- [42] G.N. Lawrence, in *Applied Optics and Optical Engineering*, edited by R.R. Shannon and J.C. Wyant (Academic, New York, 1992), Vol. 11.
- [43] ZEMAX Development Corporation, <http://www.zemax.com>.
- [44] O. Chubar and P. Elleaume, in *Proceedings of the 6th European Particle Accelerator Conference, Stockholm, 1998* (IOP, London, 1998), p. 1177.
- [45] M. Geitz, Ph.D. thesis, Hamburg University [DESY-THESIS-1999-033, 1999].
- [46] H. Delsim-Hashemi, Ph.D. thesis, Hamburg University [DESY-Thesis-2008-024, 2008].
- [47] B. Schmidt *et al.*, Proceedings of FEL08, Gyeongju (2008).
- [48] E.L. Saldin, E.A. Schneidmiller, and M.V. Yurkov, Nucl. Instrum. Methods Phys. Res., Sect. A **483**, 516 (2002).
- [49] M. Venturini, Phys. Rev. ST Accel. Beams **10**, 104401 (2007).
- [50] J. Rosenzweig *et al.*, in Proceedings of FEL08, Gyeongju (2008).
- [51] G. Berden *et al.*, in *Proceedings of the 10th European Particle Accelerator Conference, Edinburgh, Scotland, 2006* (EPS-AG, Edinburgh, Scotland, 2006).
- [52] I. Wilke *et al.*, Phys. Rev. Lett. **88**, 124801 (2002).